Mechanical, tribological and oxidation properties of high entropy nitride $(TiCrVAl)_{1-x}N_x$ coatings

Huan Luo[a], Hui Sun[b,*], Peipei Wang[a], Xing Zhao[a], Pascal Briois[c], Alain Billard[c]

[a] School of Materials Science and Engineering, Xi'an University of Science and Technology, Xi'an, 710054, China

[b] Shandong Key Laboratory of Optical Astronomy and Solar-Terrestrial Environment, School of Space Science and Physics, Shandong University, Weihai, Shandong, 264209, China

[c] Université Marie et Louis Pasteur, UTBM, CNRS, FEMTO-ST institute, F-25200, Montbéliard, France

Abstract

A dual strategy combining high-entropy composition design and microstructural engineering is employed to optimise the overall performance of protective coatings. A series of $(TiCrVAl)_{1-x}N_x$ coatings ($0.15 < x < 0.46$) is prepared by pulsed magnetron sputtering. Precise nitrogen regulation is utilised as a microstructural engineering tool to achieve the controlled transformation of coating structures within a fixed equiatomic metallic component framework. Increasing x from 0.15 to 0.46 causes a pronounced structural evolution, from an amorphous state to a nanocomposite structure, and ultimately to a well-crystallized structure. The nanocomposite structure was achieved in the $(TiCrVAl)_{0.62}N_{0.38}$ coating, delivering the highest hardness of 37.6 GPa, superior toughness (reflected by H/E^* of 0.084), and ultralow wear rate of 4.7×10^{-9} mm^3 N^{-1} m^{-1}. Oxidation tests further reveal that the $(TiCrVAl)_{0.62}N_{0.38}$ coating possesses the strongest oxidation resistance, attributed to the formation and retention of the continuous Al_2O_3 scale.

Keywords: Microstructure, Magnetron sputtering, High-entropy nitride coatings, Mechanical and tribological properties

1. Introduction

With the rapid advancement of modern manufacturing technologies, substantial human and financial resources have been continuously invested in fields such as cutting tools, high-pressure fluid processing, and aviation propulsion equipment, which are strategic pillars of the national economic development [1][2]. The long-term reliability and performance of these fields critically depend on a small number of high-value contacting components, including high-speed-machining blades, pump shafts and valves, drill-bit contact surfaces, compressor blades, and bearing raceways and gears that operate within high-temperature rotating assemblies [3][4]. These components are routinely exposed to exceptionally harsh service conditions that couple high contact stresses, high sliding velocities, repetitive impact loading, abrasive particle-laden media, and oxidation environments severe enough to compromise conventional protective layers. Such a harsh operating environment demands that the coating must achieve a synergistic combination of outstanding mechanical properties, excellent wear resistance and robust oxidation resistance. Although traditional binary and ternary nitride coatings (such as TiN, CrN, TiAlN and their multilayer films) can independently provide high hardness or excellent wear resistance, they typically fail to satisfy these coupled requirements[5][6][7]. For instance, the increased hardness is often accompanied by enhanced brittleness and reduced impact tolerance. The limited compositional tunability restricts the supply of antioxidant elements, and nanocrystalline structures promote rapid degradation under thermo-tribological loading. Therefore, there is an urgent need for coating solutions that reconcile hardness with toughness, deliver exceptional wear resistance, and simultaneously provide sufficient oxidation protection.

High-entropy nitride (HEN) coatings have attracted extensive interest due to their multicomponent synergistic effects, entropy-stabilized phases, pronounced lattice distortion, and sluggish diffusion effect [8]. These effects could simultaneously provide outstanding mechanical properties, thermal stability, and oxidation resistance [9]. Microstructural engineering has been proven to be able to address the shortcomings of incompatibility between the hardness and toughness of binary metal carbides to a certain extent by constructing dual-phase nanocomposite structures, thereby achieving excellent wear resistance [10]. However, the application of such microstructural engineering strategies in high-entropy nitride coatings remains relatively limited. Therefore, it is predicted that HEN coatings can be coupled with microstructural engineering to enable a broader design space that facilitates a more favourable balance among mechanical, tribological, and antioxidant capacity, thereby offering a promising pathway to overcome the intrinsic limitations of conventional nitride protective coatings.

Over the past decade, transition-metal-based HEN coatings, such as (AlCrMoTaTi)N [11][12], (HfNbTaTiZr)N [13], and (MoNbTaTiZr)N [14], have been extensively investigated, and they have been proven to have great application potential in fields such as moulds, marine service environments, and energy conversion devices. Jibin Pu et al. [15] studied

(VAlTiCrMo)N_x coatings based on magnetron sputtering. The results showed that increasing nitrogen content in (VAlTiCrMo)N_x drove BCC-FCC transformation and more severe lattice distortion, thus achieving the best mechanical strength and corrosion resistance (in 3.5 wt% NaCl) at the nitrogen content of 34 at.%. The TiVCrZrWN_x coating was investigated by Ping Ren et al. [16], who confirmed that its structure can be modulated by nitrogen and verified that a hardness of 21.3 GPa and a low coefficient of friction of 0.38 (in seawater medium) can be obtained simultaneously at a nitrogen flow rate of 24 sccm. In the exploration of (TiZrNbTa)N coatings, Cheng-Yi Lai et al. [17] found that the coating exhibited the highest hardness and Rp value of 23.5 GPa and 198 kΩ cm^2 when the nitrogen content was 21.5 at.%, which was provided by the dual-phase nanostructures combining M_2N-type HCP nitride and MN-type FCC nitride. According to the above-mentioned studies, the nitrogen content is a critical parameter governing the microstructure and performance of HEN coatings, as it directly determines the bonding configuration, defect density, and phase constitution. Therefore, tunable nitrogen content can be employed as an effective tool for microstructural engineering in the HEN coatings. However, despite the aforementioned significant progress, existing studies typically treat a selected metallic component or the nitrogen partial pressure during deposition as the primary variable, while lacking a rigorous distinction of the actual microstructural states of the resulting coatings. Moreover, the mechanisms by which nitrogen content drives microstructural transitions, the precise correlations between such structural evolution and the resulting properties, and the underlying physical origins remain far from being fully understood. Furthermore, the combined performance of high-entropy nitride coatings in terms of dry sliding tribological behaviour and oxidation resistance has rarely been explored. Systematic investigations that simultaneously evaluate the mechanical properties, tribological performance, and oxidation resistance of high-entropy nitride coatings are still lacking. Besides, in the high-entropy nitride system, the influence of nitrogen content on microstructure and properties is highly system-dependent. Results obtained in one nitride system cannot be straightforwardly extrapolated to another high-entropy system, which necessitates specialized and systematic investigations for specific compositions.

Among the various high-entropy nitride systems, (TiCrVAl)N shows great promising application prospects because the strong oxygen affinity of Al, the solid-solution strengthening ability of Ti, the low diffusion coefficient of Cr oxides, and the amorphization tendency and lubricating functionality of V collectively provide multiple performance advantages. These characteristics make the (TiCrVAl)N coating a unique platform for studying how high-entropy effects and microstructure engineering optimizes the comprehensive performance of protective coatings and overcome the intrinsic limitations of conventional nitride coatings. However, the systematic investigations on (TiCrVAl)N coatings remain scarce, particularly with respect to the integrated assessment of their mechanical properties, tribological behaviour, and oxidation resistance,

which has not yet been reported. Consequently, there is an urgent need to elucidate how nitrogen content governs the microstructural characteristics of (TiCrVAl)N coatings, and how such microstructural evolution synergistically dictates their mechanical response, wear behaviour, and oxidation performance under harsh service conditions.

In the present work, a series of $(TiCrVAl)_{1-x}N_x$ coatings with controlled nitrogen contents was deposited using pulsed direct-current magnetron sputtering. The adjustable nitrogen content was used as the tool to achieve the coating microstructure engineering. The microstructure of the coatings was systematically regulated, enabling a continuous microstructural evolution from an amorphous structure to a nanocomposite structure and finally to a highly crystalline FCC structure. The microstructure and morphology of the coatings were characterized by XRD, TEM/EDS, and SEM/EDS, while their chemical composition was determined by GD-OES. The systematic investigation was conducted to evaluate the influence of nitrogen-induced microstructure on the mechanical, tribological, and oxidation properties of the $(TiCrVAl)_{1-x}N_x$ coatings, and the underlying mechanisms governing the microstructure evolution and performance were discussed.

2. Experimental

The $(TiCrVAl)_{1-x}N_x$ coatings were fabricated by reactive pulsed direct current (DC) magnetron sputtering technique in an argon atmosphere using a dual-target configuration. The four metallic constituents were supplied by TiAl and CrV alloy targets with equiatomic compositions. Each target had a radius of 300 mm, a thickness of 6 mm, and a purity of 99.9 at.%. The two alloy targets were powered by the pulsed DC advanced energy dual generator, and the target-to-substrate distance was maintained at 90 mm. The composition of the $(TiCrVAl)_{1-x}N_x$ coating was regulated by adjusting the power applied to the targets and the nitrogen flow rate, with the corresponding parameters summarized in Table 1. To accommodate different characterizations and testing requirements, Si wafer (10 mm×10 mm), single-side-polished M2 (63 HRc, Ø=30 mm × 8 mm), stainless steel slide (40 mm × 20 mm × 4 mm), and stress-relieved iron bar (400 mm × 4 mm × 0.25 mm) were used as substrates. Neither substrate biasing nor additional heating was applied during the coating deposition. The deposition time for the $(TiCrVAl)_{1-x}N_x$ coating was set to 2 hours.

Table 1. The discharge parameters for the deposition of $(TiCrVAl)_{1-x}N_x$ coatings.

Target	Current (A)	Voltage (V)	Power (W)	Ar (sccm)	N_2 (sccm)	Pressure (Pa)
AlTi	2.5	313→366	782→915	200	4→12	~1.5
CrV	1.7→1.9	281→316	478→600			

Before the deposition of $(TiCrVAl)_{1-x}N_x$, the ion etching and the deposition of the TiCrVAl buffer layer were sequentially employed to enhance coating-substrate adhesion. During the deposition of the buffer layer, the power supplies connected to the AlTi and CrV targets were switched on simultaneously. The AlTi target was operated at a discharge current of 2.5 A and a discharge voltage of 366 V, with a pulse frequency of 50 kHz. The CrV target was operated at a discharge current of 1.25 A and a discharge voltage of 291 V, with the same pulse frequency of 50 kHz. The argon flow rate was maintained at 200 sccm, and the deposition time of the buffer layer was fixed at 10 mins. Besides, the target poisoning is suppressed through a closed-loop, real-time feedback control system of the N_2 flow rate based on the PID control strategy. This system consists of an optical emission spectroscopy (OES) unit for diagnosing the plasma chemical state and a PC control unit for processing the OES signals and dynamically regulating the N_2 flow rate. The OES system serves as the real-time process sensor, with the optical fiber positioned above the ionization region of the AlTi alloy target. The emission intensities of atomic nitrogen (N^*) and titanium (Ti^*) are continuously monitored, and their intensity ratio is employed as the feedback parameter to reflect the nitridation state of the target surface. The deviation between the measured signal and the setpoint is processed by the PID controller. The output of the PID controller then dynamically regulates the N_2 flow rate in real time, thereby stabilizing the reactive sputtering process and suppressing target poisoning.

The phase constitution of the $(TiCrVAl)_{1-x}N_x$ coatings, including the as-deposited state and the post-oxidation condition, was examined by X-ray diffraction (BRUKER D8, with Co source). A Co Kα radiation source with a wavelength of 1.78897 Å was employed, with the accelerating voltage of 35 kV and tube current of 40 mA. Diffraction patterns were recorded in air over a 2θ range from 20° to 100°, using a continuous scanning mode with a step rate of 0.1° s^{-1}. The chemical composition was tested by glow discharge optical emission spectrometry (GD-OES) [18]. The thickness, surface and cross-sectional morphology, and distribution of each component element of the coating in the deposited state and after oxidation were characterized by SEM coupled with EDS (JEOL JSM-7800F). More detailed information on the coating microstructure was obtained by TEM (FEI Talos F200X-G2, with Super-X EDS). The samples for TEM characterizations were prepared by a FIB-SEM double beam system (FEI, Helios Nano Lab 600i) operating at 2-30 kV. The gallium ion beam was operated at a voltage of 30 kV, which was mainly used to slice the samples at a micro-nano scale. The residual stress was evaluated by measuring the curvature radius of coatings deposited on a stress-relieved iron bar with dimensions of 400 mm × 4 mm × 0.25 mm. Before the deposition process, the iron bar substrate was annealed for 2 hours to eliminate the initial residual stress, thereby ensuring a zero-curvature condition and avoiding potential errors in the subsequent curvature measurements. Upon completion of the coating deposition, the curvature radius (R) of the coated iron bar was measured using an Altysurf

profilometer equipped with an optical probe. The residual stress in the as-deposited $(TiCrVAl)_{1-x}N_x$ coating was then calculated from the measured curvature radius using Stoney's equation,

$$\sigma = \frac{E_S}{6(1-\upsilon_S)}\frac{d_S^2}{d_C}\frac{1}{R}.$$

In this equation, E_s, d_s, and v_s represent the Young's modulus, thickness, and Poisson's ratio of the substrate, respectively, whereas d_c denotes the coating thickness and R corresponds to the measured curvature radius. The hardness and Young's modulus of the coatings were measured by using a nanoindenter (CSM Instruments equipped with the Berkovich diamond indenter tip), and the detailed testing parameters and procedures can be found in [18]. The tribological properties were evaluated using a pin-on-disk tribometer (CSM, Switzerland). All tests were conducted under dry sliding conditions in ambient air at room temperature (~22 °C) with a relative humidity of approximately 36%, using a WC/Co ball with a diameter of 6 mm. The applied normal load was fixed at 5 N, while the sliding speed was set to 10 cm/s along a circular wear track with a radius of 5 mm. Each test was performed for 10000 sliding cycles. After the tribological test, the cross-sectional profiles of the wear tracks were measured using an Altysurf profilometer (Altisurf 500) equipped with a tungsten micro-force inductive probe, providing an accuracy of about 20 nm. The normalized wear rate (W_r) was calculated according to the formula $W_r=V/(F\times L)$, where V represents the wear volume (mm^3), F is the applied normal load (N), and L denotes the total sliding distance (m). The oxidation performance was assessed through annealing-cooling cycles conducted in air using a high-temperature furnace (Borel TL 1100-8). Each annealing temperature, ranging from 200 °C to 800 °C in 100 °C increments, was reached at a heating rate of 100 °C/h and maintained for 2 h. After the oxidation test, the sample remained in the furnace and cooled naturally to room temperature along with the furnace.

3. Results and discussion

3.1 Chemical composition and microstructural evolution

Figure 1 presents the chemical compositions of the $(TiCrVAl)_{1-x}N_x$ coatings deposited under various nitrogen flow rates. It is evident that across all the coatings with various nitrogen content, the four metallic constituents maintain an approximately equiatomic ratio. Notably, the compositional difference between Ti and Al progressively narrows, reaching an exact equiatomic ratio at 46 at.% nitrogen content, in agreement with the target composition. The Cr content remains slightly higher than that of V at all nitrogen levels.

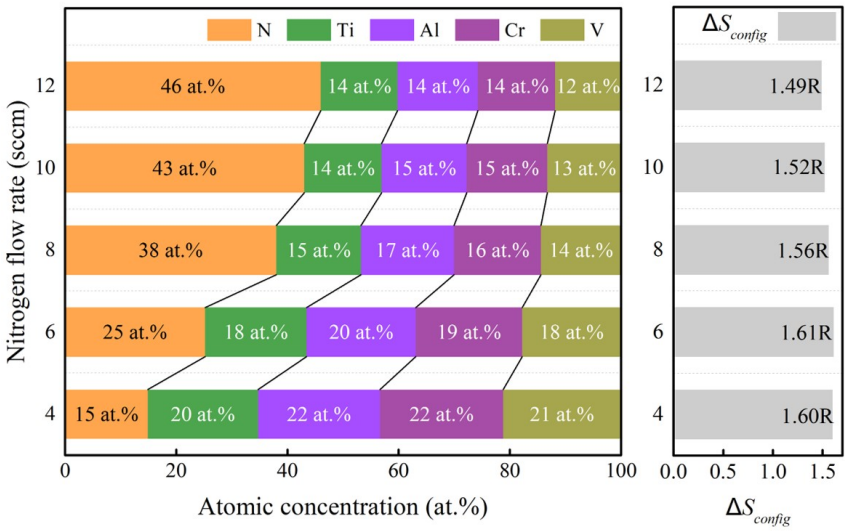

Figure 1. Chemical compositions of $(TiCrVAl)_{1-x}N_x$ coatings with various nitrogen flow rates deposited on stainless steel substrates.

During the preparation of $(TiCrVAl)_{1-x}N_x$ coatings, equiatomic TiAl alloy and CrV alloy targets were employed. In general, the final chemical composition fabricated by magnetron sputtering is governed by several factors, such as sputtering yield, atomic mass of the target elements, and their transport behaviour in the plasma [19]. In the present case, although Al exhibits a sputtering yield nearly 40% higher than Ti, its larger thermal velocity and shorter residence time in the plasma lead to a lower ionization probability and greater escape losses. These offset part of the compositional gain from its higher sputtering yield. Consequently, at a nitrogen flow rate below 10 sccm, the Al content remains slightly higher than Ti, preserving an approximately equiatomic balance. With increasing nitrogen flow rate, the plasma collision probability in the ionization region rises, causing lighter Al atoms to undergo more frequent scattering, momentum loss, and deviations from their transport trajectories (alterations in the direction toward the substrate) during collisions [20]. As a result, the total flux of Al species reaching the substrate is reduced to a certain extent. For comparison, Ti atoms, with higher atomic mass, retain greater inertia, making their momentum transfer and trajectory less susceptible to collisional effects. Therefore, at 12 sccm nitrogen flow rate, Ti and Al concentrations become equal.

For Cr and V, across all nitrogen flow rates, the Cr content remains slightly higher than that of V, showing a minor deviation from the target composition. It is known that Cr and V have comparable ionization probabilities, while Cr possesses slightly higher atomic mass and sputtering yield. Unlike Al, Cr possesses both a high atomic mass and a high sputtering yield. Regardless of the nitrogen flow rate, the higher mass of Cr renders it less susceptible to the adverse effects of elastic collisions than V when sputtered from the CrV target, especially in terms of transport trajectory deviation and kinetic energy

loss. Consequently, the intrinsically higher sputtering yield of Cr cannot be attenuated by the progressively increased collision probability, and thus Cr remains slightly enriched in the coating across all nitrogen flow rates. Overall, despite minor variations among the metallic components, their overall composition remains near-equiatomic proportions, aligning with the high-entropy design principle. In addition to the four metallic components, it is also observed that the nitrogen incorporation rises rapidly from 15 at.% to 38 at.% as the nitrogen flow rate increases from 4 sccm to 8 sccm. However, the increase slows to only 3 at.% when the nitrogen flow rate is further raises from 10 sccm to 12 sccm. Even at the highest nitrogen flow rate of 12 sccm, the nitrogen content occupying anion sites remains below 50 at.%, indicating the sub-stoichiometric nitride state. Based on the above determination of the chemical composition, all coatings are labelled as $(TiCrVAl)_{1-x}N_x$, where x = 0.15, 0.25, 0.38, 0.43, and 0.46.

Figure 2(a) shows the XRD patterns of the $(TiCrVAl)_{1-x}N_x$ coatings with x ranging from 0.15 to 0.46 deposited on M2 steel. It is clearly observed that with increasing x value, the $(TiCrVAl)_{1-x}N_x$ coating structure transitions from an amorphous state to a nanocrystalline state, followed by a gradual enhancement in crystallinity. For the coatings with x =0.15 and 0.25, the structures exhibit amorphous characteristics. It is attributed to the insufficient nitrogen occupancy under the low nitrogen atmosphere, which suppresses the establishment of long-range order of metal-nitrogen bonding and impedes lattice stabilization [21]. Consequently, atoms arriving at the substrate surface undergo random packing, yielding a disordered amorphous configuration. Meanwhile, the disordering favoured by the high configurational entropy at the low nitrogen content (Fig. 1(b)) increases the nucleation barrier, which also keeps the coating structure in the amorphous state. When the x value increases to 0.38, the coating evolves into a nanocrystalline structure, characterized by the typical single-phase FCC structure without any secondary phases, as evidenced by diffraction peaks located at 44.5°, 51.6°, and 97.8°. This suggests that the nitrogen content of 38 at.% surpasses the crystallization kinetics threshold of the Ti-Al-Cr-V-N system, enabling the formation and stabilization of crystal nuclei. However, the sluggish diffusion effect intrinsic to the high-entropy system may simultaneously suppress grain coarsening [22][23]. These factors collectively promote locally ordered atomic arrangements and thus drive the progressive evolution toward a nanocrystalline structure. With a further increase in x from 0.38 to 0.46, the intensity of the (111) peak is significantly enhanced, indicating a substantial improvement in crystallinity. This marked crystallinity improvement at higher nitrogen levels originates from both thermodynamic and kinetic contributions. From the thermodynamic perspective, the elevated nitrogen content lowers the interfacial free energy of crystal nuclei, thereby facilitating atomic migration and rearrangement into more ordered structures, which in turn strengthens crystallinity [24]. From the kinetic perspective, the target poisoning induced by the high-nitrogen atmosphere decreases the metal particle flux

sputtered from the target surface, allowing the adatoms reaching the substrate sufficient time to diffuse to low-energy sites, thereby leading to improved crystallinity [25]. Besides, note that the rather weak peak at 39.5° is associated with the K_β radiation of the Co source, originating from the intense FCC (111) peak. The (110) plane of the Fe peak (PDF#06-0696) at 52.2° is contributed by the M2 steel substrate, marked by the grey circle.

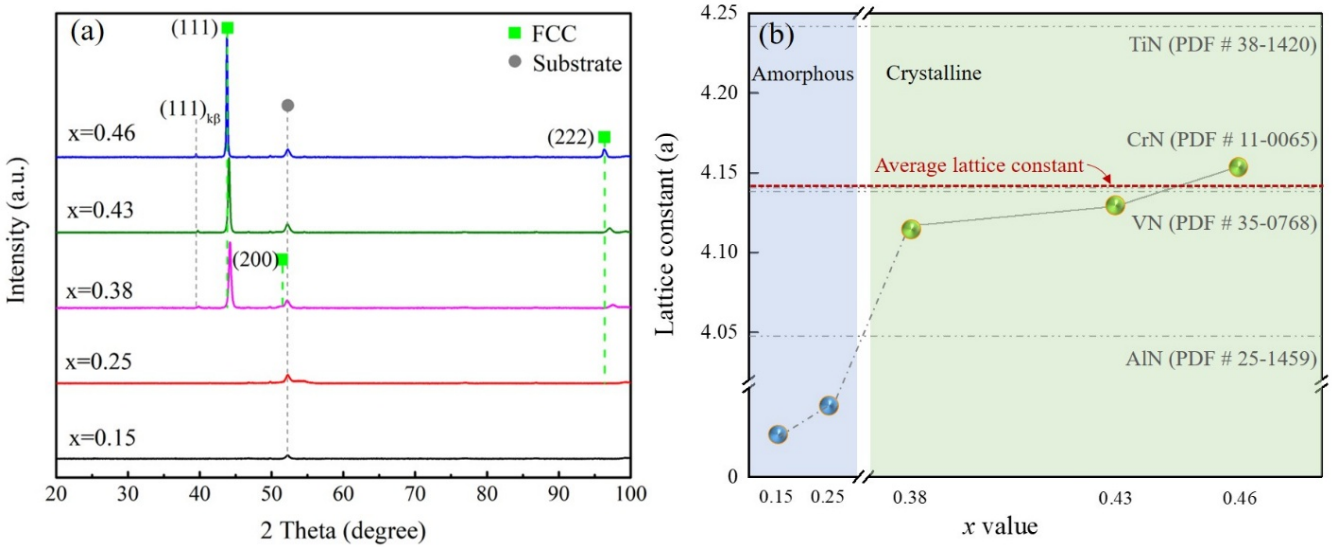

Figure 2. (a) X-ray diffraction patterns and (b) lattice constants of $(TiCrVAl)_{1-x}N_x$ coatings with x = 0.15-0.46 deposited on M2 substrates.

In addition to the overall evolution trend of the coating structure, it can be observed that as the x value increases from 0.38 to 0.46, the diffraction peaks show intensity enhancement and narrowing of half-peak width, accompanied by an obvious low-angle shift. On the one hand, the narrowing and strengthening of XRD peaks indicate the grain coarsening and crystallinity enhancement of the coating. Based on the calculation of Scherrer's formula [26], the grain size increases from 29.8 nm, 35.4 nm to 60 nm when the x value changes from 0.38, 0.43 to 0.46. On the other hand, the low-angle shift corresponds to an increase in the lattice constant (shown in Fig. 2(b)), which is attributed to the expansion of interplanar spacing caused by the continuous incorporation of nitrogen atoms. In general, the low-angle shift of diffraction peaks also originates from the accumulation of compressive stress within the coating. However, as shown in Fig. 3, the compressive stress of $(TiCrVAl)_{1-x}N_x$ coatings decreases as the x value increases from 0.38 to 0.43. It normally induces a shift toward the higher angle, in complete contrast to the evolution trend of XRD. It suggests that nitrogen incorporation plays a more critical role than stress accumulation in controlling the lattice expansion in the $(TiCrVAl)_{1-x}N_x$ coatings. The lattice constant calculated from the (111) peak using Bragg's law [27] increases from 4.12 Å to 4.15 Å as x increases from 0.38 to 0.46. The standard lattice constants of binary nitrides corresponding to each metal component in the $(TiCrVAl)_{1-x}N_x$ coating are 4.242

Å (TiN, PDF# 38-1420), 4.140 Å (CrN, PDF# 11-0065), 4.139 Å (VN, PDF# 35-0768) and 4.045 Å (AlN, PDF# 25-1459), respectively. Their average value is 4.142 Å and is marked by the red dashed line in Fig. 2(b). It can be seen that as the dissolved N atoms increase, the lattice constant of $(TiCrVAl)_{1-x}N_x$ coating gradually approaches the average value of all constituents, and then exceeds the average value at $x = 0.46$. This indicates that for the Ti-Al-Cr-V-N system with N content exceeding 43 at.%, the atomic size mismatch and bonding heterogeneity lead to the elongation of average bond length, thus resulting in a positive deviation in the lattice constant.

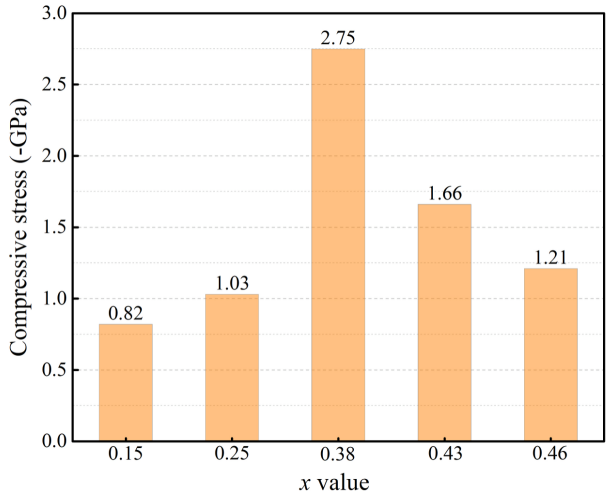

Figure 3. Residual stress evolution of $(TiCrVAl)_{1-x}N_x$ coatings with $x = 0.15$-0.46 deposited on iron bar substrates.

Figure 3 shows the compressive stress evolution of $(TiCrVAl)_{1-x}N_x$ coatings with different x values. With increasing x, the residual compressive stress first increases and then decreases. For the deposition process without substrate heating, in our case, the residual stress in the $(TiCrVAl)_{1-x}N_x$ coatings is mainly controlled by the plasma bombardment effect, chemical (nitridation) strain and microstructural changes. As x increases from 0.15 to 0.38, the elevated plasma density and nitrogen incorporation enhance the ion bombardment and nitridation reaction, which generates a large number of dislocations, interstitial atoms, and chemical strains that are difficult to relax due to the sluggish diffusion effect, thereby leading to the accumulation of substantial compressive stress [28][29]. However, when the x exceeds 0.38, the ion bombardment effect declines, resulting in a reduction of compressive stress. Meanwhile, at high nitrogen levels, the crystallization process and microstructural coarsening (Fig. 4) promote defect annihilation and stress relaxation, which further contribute to the decrease of compressive stress.

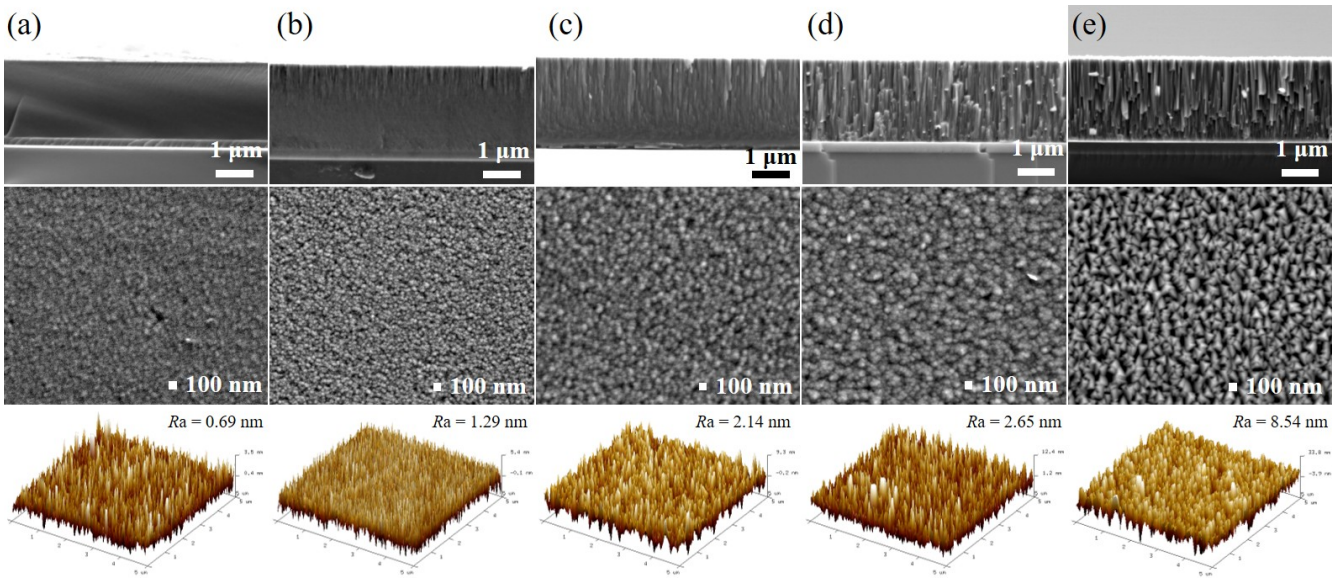

Figure 4. Plan-view and cross-sectional SEM micrographs and AFM surface topographies of $(TiCrVAl)_{1-x}N_x$ coatings with varying x value deposited on Si wafer substrates: (a) x = 0.15, (b) x = 0.25, (c) x = 0.38, (d) x = 0.43 and (e) x = 0.46.

The cross-sectional and plan-view SEM micrographs and AFM surface topographies (Fig. 4) reveal a distinct morphology evolution of the $(TiCrVAl)_{1-x}N_x$ coatings with increasing x value. At x = 0.15 and 0.25, the coating displays a fine-grained surface with average surface roughness (Ra) values of 0.69 nm and 1.29 nm, respectively, and has a compact, glassy structureless cross-section, indicative of amorphous characteristics. With moderate N incorporation x = 0.38, the dense and vertically aligned fine columns emerge, while the surface remains relatively smooth, with weak grain contrast and a roughness of 2.14 nm. Upon further N increase, x = 0.43, the columns coarsen and the surface develops more pronounced granular features. At the highest N content x = 0.46, the coating presents coarser columnar crystals and the intercolumnar gaps and a roughened, faceted surface become apparent (R_a increases to 8.54 nm), evidencing shadowing-dominated growth and locally reduced densification. Overall, the $(TiCrVAl)_{1-x}N_x$ coatings evolve from amorphous to dense nanocolumnar and ultimately to coarse columnar structure with intercolumnar gaps. This evolution arises from the synergistic effects of anion occupation and coating growth kinetics. Specifically, increasing nitrogen strengthens metal-nitrogen bonding and stabilizes the crystal lattice, which enables the morphological transition from glassy to nanocolumnar crystals. Simultaneously, target poisoning at moderate N flow rate reduces metal flux and enhances the diffusion-to-arrival ratio of adatoms, yielding dense, fine columnar growth. At higher N contents, however, increased plasma collisions dissipate ion energy and broaden the angular distribution of incident species, thereby promoting self-shadowing and porosity [30][31].

To further elucidate the cross-sectional microstructure and morphological evolution beyond XRD and SEM, transmission electron microscopy (TEM) is employed. It is noteworthy that the coating with x = 0.38 represents the first sample undergoing the transition from amorphous to crystalline state, characterized by the weakest crystallinity and suggesting the possible presence of an amorphous phase. Therefore, the $(TiCrVAl)_{0.62}N_{0.38}$ coating is preferentially selected as the representative sample for TEM, shown in Fig. 5. Along the growth direction, the fine and dense columnar crystal structure without discernible inter- and intra-columnar gaps is clearly observed (Fig. 5(a) and (b)). EDS mapping confirms the homogeneous distribution of each metallic component and nitrogen element (Fig. 5(c)), with no evidence of elemental clustering or segregation even at the columnar boundaries. High-resolution images (Fig. 5(d)) provide direct evidence of the nanocomposite structure of the $(TiCrVAl)_{0.62}N_{0.38}$ coating, where distinct lattice fringes coexist with disordered stacked amorphous structures (highlighted by yellow ellipses). The corresponding SAED pattern (Fig. 5(e)) identifies that the crystalline domains belong to the FCC phase. Its polycrystalline diffraction rings are indexed as the (111), (200), (220), (311), and (222) planes, in agreement with XRD results. Furthermore, magnified HRTEM images (Fig. 5(f1, g1)) of the two regions marked by red rectangles in Fig. 5(d) are unambiguously identified as (111) and (200) planes, exhibiting lattice spacings of 0.236 nm and 0.206 nm, respectively. Meanwhile, the corresponding inverse fast Fourier transform (IFFT) images (Fig. 5(f2, g2)) display severely distorted lattice fringes and dislocation distribution. The amorphous domains in the nanocomposite structure, highlighted by yellow ellipses, are further confirmed by the broadened diffuse halo obtained via IFFT.

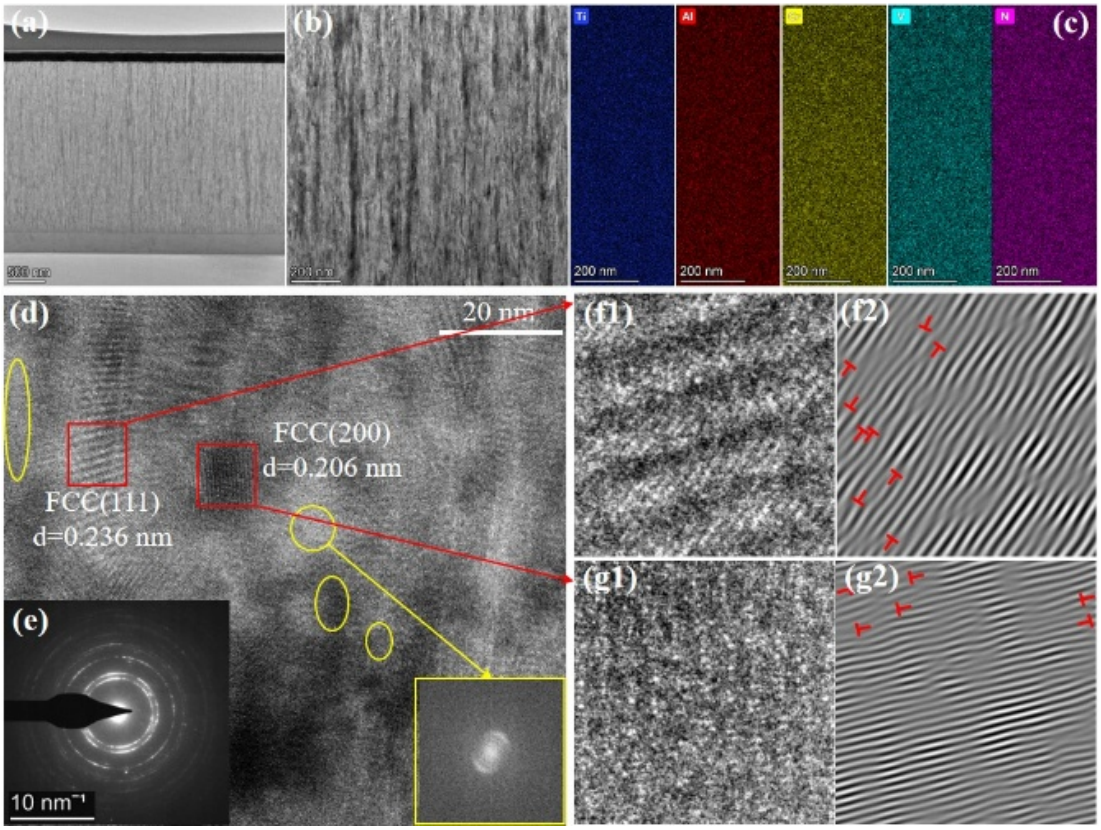

Figure 5. (a) and (b) Cross-sectional TEM images with different magnifications, (c) EDS element mapping, (d) BF-TEM image with (e) the SAED pattern, (f1, g1) enlarged HRTEM images taken from the red rectangular area, (g1, g2) IFFT taken from (f2, g2) of the $(TiCrVAl)_{0.62}N_{0.38}$ coating deposited on Si wafer substrates.

Based on the XRD results, it is already known that the crystallinity of $(TiCrVAl)_{1-x}N_x$ coatings increases with the increase of x value. To determine whether the coating could maintain the nanocomposite structure at a higher nitrogen content $x > 0.38$, the TEM of the $(TiCrVAl)_{0.54}N_{0.46}$ coating is carried out. Unlike the dense and fine columnar structure observed in $(TiCrVAl)_{0.62}N_{0.38}$, the $(TiCrVAl)_{0.54}N_{0.46}$ coating exhibits pronounced column coarsening (Fig. 6(a)) and a loose columnar crystal feature with obvious intercolumnar gaps (indicated by the orange arrows in Fig. 6(b)). Nevertheless, EDS mapping confirms that all metallic components and nitrogen remain uniformly distributed throughout the coating (Fig. 6(c)). High-resolution TEM image (Fig. 6(d)) reveals extensive, well-defined crystalline regions in which no disordered amorphous domains are observed. The corresponding SAED (Fig. 6(e)) displays brighter and sharper FCC diffraction rings, which are indexed to the (111), (200), (220) and (222) crystal planes. The above two observations jointly confirm that the coating has transitioned from a nanocomposite structure to a well-crystallized FCC phase. In addition, from the large-area crystalline structure without a second-phase interface and the SEAD pattern, it can be inferred that the disappearance of the amorphous

phase promotes the coarsening of crystalline grains, which is consistent with the grain size evolution calculated by XRD. The magnified HRTEM images of two selected crystalline regions (Fig. 6(f1, g1)) show distinct lattice fringes, both with the interplanar spacing of 0.240 nm, corresponding to the FCC (111) plane. The corresponding IFFT analysis (Fig. 6(f2, g2)) reveal localized lattice distortions and dislocations, which are less in contrast to the $(TiCrVAl)_{0.62}N_{0.38}$ coating.

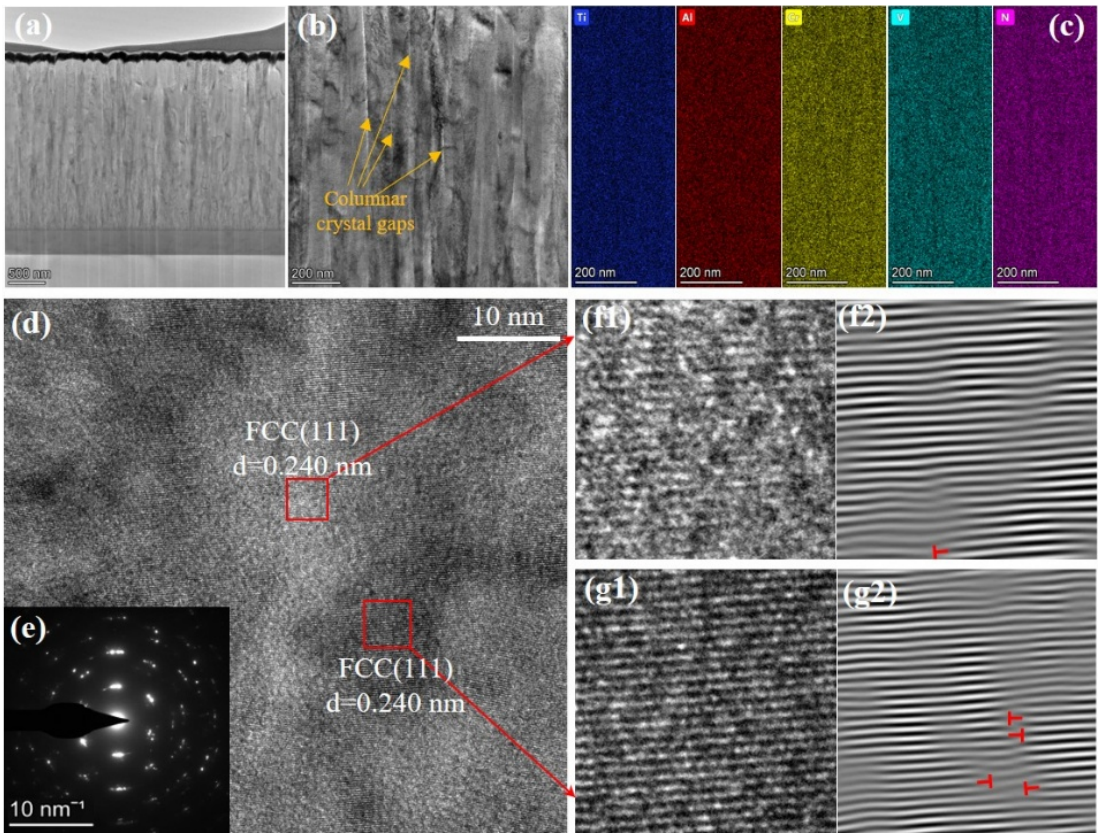

Figure 6. (a) and (b) Cross-sectional TEM images with different magnifications, (c) EDS element mapping, (d) BF-TEM image with (e) the SAED pattern, (f1, g1) enlarged HRTEM images taken from the red rectangular area, (g1, g2) IFFT taken from (f2, g2) of the $(TiCrVAl)_{0.54}N_{0.46}$ coating deposited on Si wafer substrates.

Combining the results of XRD and TEM, it can be determined that with the progressive incorporation of N atoms into the Ti-Al-Cr-V system, the $(TiCrVAl)_{1-x}N_x$ coating gradually transitions from the amorphous structure to the nanocomposite structure, and finally converts to the well-crystalline FCC phase. On the one hand, the introduction of N atoms facilitates the formation of strong metal-nitrogen bonds, which promote the conversion of part of the amorphous phase (characterized by the disordered stacking of components) into the crystalline FCC phase, forming a nanocomposite structure. With further enrichment of nitride bonding, the amorphous fraction is completely sacrificed, ultimately leading to a fully crystallized structure. On the other hand, the increase in mixing entropy enhances the degree of disorder and confusion in the atomic

stacking form, thereby impeding the nucleation and growth of crystalline phases [32]. As shown in Fig. 1(b), the configurational entropy of the $(TiCrVAl)_{1-x}N_x$ coatings decreases monotonically with increasing x, which in turn explains the progressive enhancement of crystallinity as the x value increases from 0.15 to 0.46 [33].

3.2 Mechanical properties

Figure 7(a) illustrates the variation of hardness (H) and effective Young's modulus (E^*) of the $(TiCrVAl)_{1-x}N_x$ coatings as a function of x value. A progressive increase in hardness is observed with increasing x, rising from 16.3 GPa at x = 0.15 to a peak value of 37.6 GPa at x = 0.38. However, a further increase in x results in a pronounced decline, with hardness dropping to 15.3 GPa at x = 0.46. A similar evolution is observed for the effective Young's modulus E^*, which initially rises from 250 GPa at x = 0.15 to 449 GPa at x = 0.38, and subsequently decreases to 318 GPa at x = 0.46.

At low x value of 0.15, the coating is glassy and poorly ordered, while the free volume is high and the metal-nitrogen bonding is incomplete. Thus, the average bond stiffness within the $(TiCrVAl)_{0.85}N_{0.15}$ coating is relatively low, and there is no crystal structure to resist plastic flow, resulting in low hardness and low effective Young's modulus. As x increases to 0.25, the increase in hardness and effective Young's modulus results from the increase in robust metal-nitrogen bonds, which increases local bond stiffness and shear resistance. When x = 0.38, the nanocomposite structure (grain size $\approx$ 29.8 nm, evidenced by XRD) and the dense nanocolumnar morphology (shown in SEM) are formed. Under this condition, multiple strengthening mechanisms act synergistically to produce maximum hardness. First, the strengthened M-N bonding, the multi-component solid-solution and the associated severe lattice distortion increase the barrier for dislocation nucleation and motion at the atomic scale [34]. Second, the high density of nanocrystalline/amorphous interfaces and fine grainboundaries strongly impede dislocation propagation [33]. Third, the microstructural densification (dense nanocolumnar crystals) and strong compressive stress further raise the contact resistance to indentation at the microscopic scale [35]. The above three mechanisms, with different scales from atomic-level interactions to microscopic structures, produce the maximum values of H and E^* in the $(TiCrVAl)_{0.62}N_{0.38}$ coating. Further N enrichment (x = 0.43 and 0.46) shifts the structure balance towards grain coarsening (from 35.4 nm to 60 nm), columnar crystal broadening and porosity, as well as compressive stress relaxation (Fig. 3). Grain coarsening reduces the interface density and weakens its resistance to dislocation movement, while the advent of intercolumnar gaps lowers the effective load-bearing area and elastic stiffness, producing a pronounced drop in H and E^*. Meanwhile, the stress relaxation and morphology loosening also lead to a sharp decrease in coating hardness. This trend clearly demonstrates that the mechanical performance of $(TiCrVAl)_{1-x}N_x$ coatings is highly sensitive to compositional tuning, governed by the interplay between atomic-scale bonding characteristics and microstructural evolution.

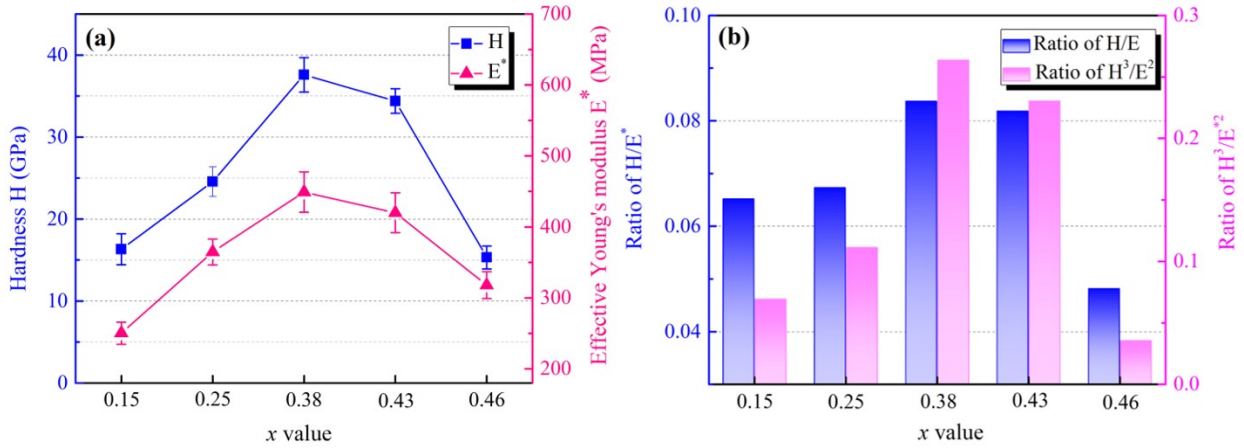

Figure 7. (a) Hardness H, effective Young's modulus E^* and (b) H/E^* and H^3/E^{*2} ratios of $(TiCrVAl)_{1-x}N_x$ coatings with x = 0.15-0.46 deposited on M2 substrates.

Figure 7(b) illustrates the evolution of H/E^* and H^3/E^{*2} ratios of $(TiCrVAl)_{1-x}N_x$ coatings. Both parameters exhibit a pronounced maximum at x = 0.38, where the H/E^* ratio reaches its highest level of ~0.084 and the H^3/E^{*2} ratio exceeds 0.26 GPa. It indicates the substantial enhancement in the $(TiCrVAl)_{0.62}N_{0.38}$ coating's ability to resist elastic strain to failure and plastic deformation, supported by the optimized balance between hardness and toughness. This favourable toughness on the basis of high hardness is associated with the amorphous phase (i.e., interface phase) distributed between the nanocrystals. On the one hand, it provides high-density interphase interfaces that hinder dislocation motion and absorb/scatter crack energy. On the other hand, it could dissipate energy and blunt the crack tip through its own local plastic deformation, thereby markedly enhancing crack resistance (indexed by H/E^*). As x continues to increase to 0.43 and 0.46, both ratios undergo a distinct decrease, even falling below the values measured at x = 0.15, indicating the deterioration in the coating's wear resistance under friction contact [36][37][38].

3.3 Tribological performance

Figure 8 presents the evolution of the dynamic friction curves, average coefficients of friction (COF), and wear rates of the $(TiCrVAl)_{1-x}N_x$ coatings as a function of x value. As shown in Fig. 8(a), all coatings exhibit a pronounced running-in stage (500-2000 laps), followed by a relatively stable steady-state regime (>2000/3000 laps). As x increases from 0.15 to 0.46, the form of the running-in stage evolves from a long and intense fluctuation characteristic (~3000 laps) to a rapid stabilization state (<500 laps). Meanwhile, the steady-state COF value and the fluctuation amplitude of the dynamic friction curve decrease progressively, indicating a lower and more stable COF at higher nitrogen contents.

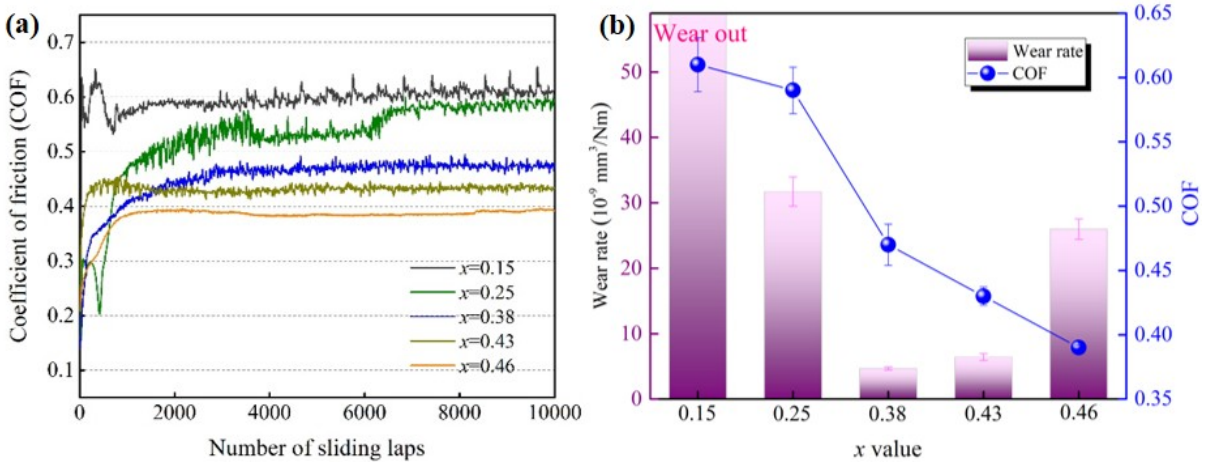

Figure 8. (a) The dynamic friction curve varied with sliding cycles and (b) steady-state coefficient of friction, wear rate of the $(TiCrVAl)_{1-x}N_x$ coatings with x = 0.15-0.46 deposited on M2 substrates.

For the coating with x = 0.15, the COF curve displays a sharp peak in the early running-in stage, followed by a steady-state segment with pronounced glitches. It suggests that the coating undergoes complete mechanical failure and wear-through in the early stage of the friction experiment. The failed coating fragments and particles act as third bodies in the subsequent cyclic sliding process, resulting in unstable contact and severe fluctuations in the friction coefficient curve. Upon increasing x to 0.25, the COF slightly decreases to 0.59. However, no abrupt peak is observed during either the running-in or steady-state stages, suggesting that the $(TiCrVAl)_{0.75}N_{0.25}$ coating remains intact throughout sliding. The relatively long running-in period and curve fluctuations are both attributed to the metallic nature (i.e., insufficient mechanical robustness) of the $(TiCrVAl)_{0.75}N_{0.25}$ coating. It leads to adhesion, local plastic deformation and abrasive wear during cyclic contact, thus causing the fluctuation of the friction coefficient. Note that the phenomenon of "low plateau to high plateau" that occurs in the latter part of the friction curve is likely related to the short-term low friction caused by a temporarily formed thin tribo-layer. However, as the sliding cycle proceeds, this tribo-layer may eventually break down into oxide debris, and the COF increases again.

As x further increases from 0.38, 0.43 to 0.46, the steady-state COF gradually decreases from 0.47 to 0.43 and eventually to 0.39, accompanied by progressively weakened glitches and shortened running-in stages. Such a trend toward lower and more stable COFs suggests a transition of the dominant wear mechanism from adhesion and abrasion to oxidation. Specifically, the gradual incorporation of nitrogen may lead to the formation of an increasingly stable oxynitride-based self-lubricating tribo layer at the sliding interface, which reduces interfacial shear stresses and suppresses both adhesion and ploughing, thereby facilitating smoother interfacial sliding. Up to x = 0.46, the dynamic COF curve exhibits a particularly

smooth profile, demonstrating the superior frictional performance of the $(TiCrVAl)_{0.54}N_{0.46}$ coating. Overall, it can be concluded that the friction coefficient of $(TiCrVAl)_{1-x}N_x$ is governed by the friction-activated chemical reactions (i.e., shear characteristics of the interfacial layer), which are monotonically improved with increasing nitrogen content.

As shown in Fig. 8 (b), the wear rates of the $(TiCrVAl)_{1-x}N_x$ coatings are presented in the form of bar charts. Excluding the completely worn-through $(TiCrVAl)_{0.85}N_{0.15}$ coating, the wear rate of the remaining coatings first decreases and then increases with increasing x value, reaching its minimum value of 4.7×10^{-9} mm³/N·m at $x = 0.38$. Obviously, the evolution trend of wear rate differs from that of COF. To clarify the mechanisms governing the wear behaviour of the $(TiCrVAl)_{1-x}N_x$ coatings, the wear track morphologies and corresponding EDS analyses are presented in Fig. 9.

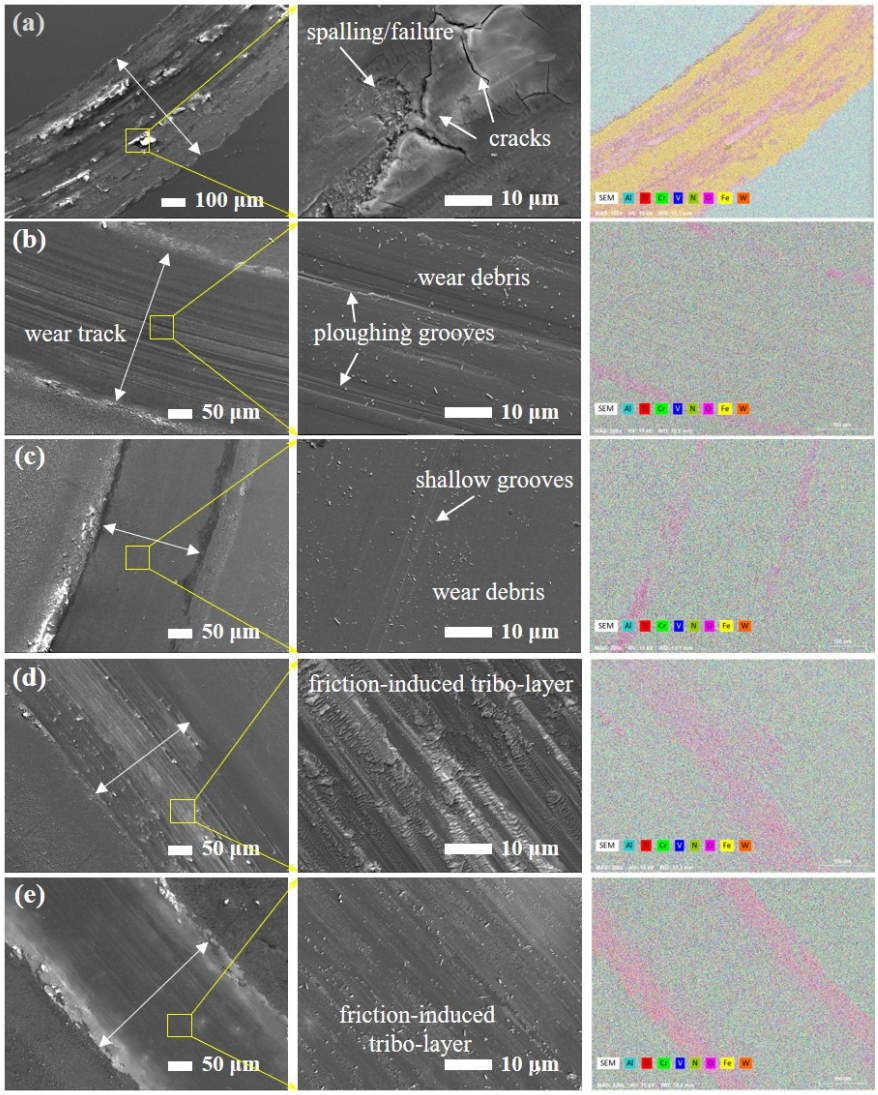

Figure 9. SEM micrographs and surface elements mappings of the wear tracks on the $(TiCrVAl)_{1-x}N_x$ coatings deposited on M2 substrates against WC/Co balls: (a) $x = 0.15$, (b) $x = 0.25$, (c) $x = 0.38$, (d) $x = 0.43$ and (e) $x = 0.46$.

When x = 0.15, the $(TiCrVAl)_{0.85}N_{0.15}$ coating is completely worn through at the early stage of the wear test (Fig. 8(a)). This is confirmed by the SEM morphology showing severe surface damage with large-area cracking and spallation, as well as by the EDS mapping detecting Fe signal that derived from M2 substrate (Fig. 9). According to the characteristics of the delamination pits formed by material transfer, it can be determined that the $(TiCrVAl)_{0.85}N_{0.15}$ coating exhibits a typical adhesive wear behaviour. Under dry sliding conditions, it is intrinsically linked to the metallic bonding character of $(TiCrVAl)_{0.85}N_{0.15}$ coating. This metallic nature promotes strong interfacial adhesion and facilitates shear transmission into the subsurface during cyclic loading, thereby accelerating fatigue damage accumulation and ultimately leading to coating delamination. Therefore, for the $(TiCrVAl)_{0.85}N_{0.15}$ coating, the synergistic effect between adhesion-induced shear and cyclic fatigue governs the wear behavior rather than mechanical properties alone. When x = 0.25, the $(TiCrVAl)_{0.75}N_{0.25}$ coating remains intact after testing, and the wear rate reduces to approximately 3.2×10^{-8} mm³/N·m. The wear track shows pronounced ploughing grooves along the sliding direction and several wear debris, some of which adhere to the wear track surface. These features indicate an abrasive wear dominated by third-body effects. As x increases to 0.38, the wear rate reaches its minimum, while the wear track exhibits the narrowest width, the shallowest grooves, and the least debris accumulation. Within the range of x = 0.25 to 0.38, the enhanced wear resistance of $(TiCrVAl)_{1-x}N_x$ coatings is attributed to the improved mechanical properties, increased compressive stress and crystalline/amorphous nanocomposite structure, which provides a favourable balance between high hardness and moderate toughness. This enables the coating to resist plastic deformation, crack initiation, and fatigue spallation during sliding contact.

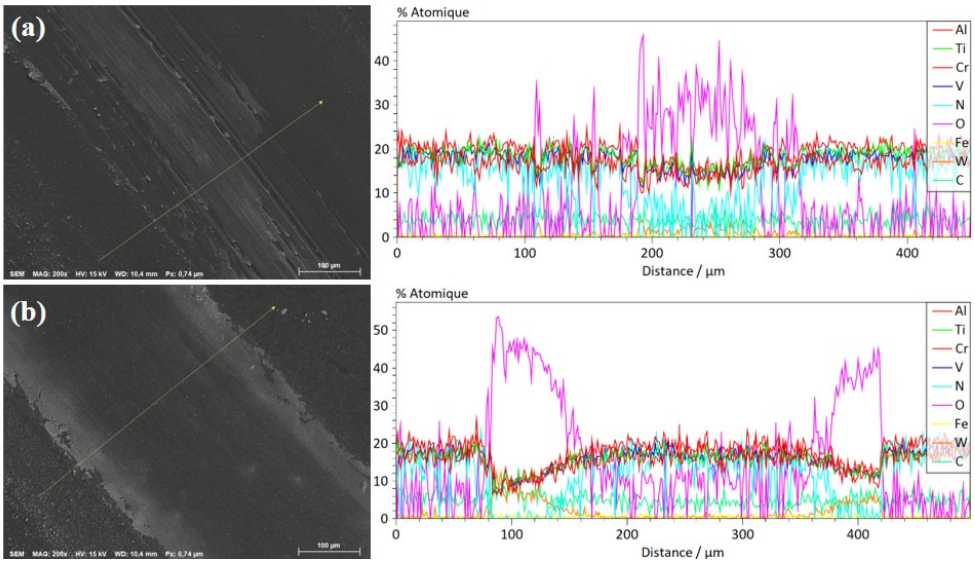

Figure 10. The line scanning analysis of the elemental composition spanning the wear tracks of $(TiCrVAl)_{1-x}N_x$ coatings deposited on M2 substrates: (a) x = 0.43, (b) x = 0.46.

As x further increases to 0.43 and 0.46, the wear rates increase again. The wear tracks become wider and new morphological features appear on them, where the tribo-layers gradually form (Fig. 9(d), (e)). For $(TiCrVAl)_{0.57}N_{0.43}$ coating, a large-area oxide layer appears in the central region of the wear track (Fig. 10(a)), accompanied by a renewed deepening of the ploughing grooves. This phenomenon results from the friction-induced chemical reaction and the reduction in hardness. For $(TiCrVAl)_{0.54}N_{0.46}$ coating, the wear track exhibits a smooth morphology without visible grooves. Notably, although the typical features of abrasive wear almost disappear, the wear rate continues to increase. This behaviour mainly arises from the insufficient mechanical strength, reduced compressive stress, and the columnar microstructure with inter-gaps at x = 0.46, all of which are detrimental to wear resistance. It is worth noting that although the mechanical properties of the $(TiCrVAl)_{0.54}N_{0.46}$ coating are weaker than those of the $(TiCrVAl)_{0.85}N_{0.15}$ coating, it remains intact after wear testing, exhibiting superior wear resistance compared to the $(TiCrVAl)_{0.85}N_{0.15}$ coating. This is because the $(TiCrVAl)_{0.54}N_{0.46}$ coating possesses strong nitride covalent bonding characteristics, which are beneficial for improving crack propagation resistance and suppressing adhesive junction and fatigue damage. Therefore, even though the $(TiCrVAl)_{0.54}N_{0.46}$ coating has lower H, H/E^*, and H^3/E^{*2} values compared to the $(TiCrVAl)_{0.85}N_{0.15}$ coating, it exhibits a superior wear rate. In addition, the smooth surface of the wear track on the $(TiCrVAl)_{0.54}N_{0.46}$ coating appears to result from the coverage of the in-situ-formed oxynitride-based tribo layer activated by friction (Fig. 10(b)). Although this tribo-layer cannot prevent material loss, it reduces the COF of the $(TiCrVAl)_{1-x}N_x$ coatings, providing direct evidence for the monotonic decrease in COF with increasing nitrogen content. In summary, the wear rate of $(TiCrVAl)_{1-x}N_x$ coatings is governed by their mechanical properties, bonding characteristics, and microstructure. The nanocomposite structure of the $(TiCrVAl)_{0.62}N_{.38}$ coating offers superior mechanical performance, composite structure and favourable compressive stress distribution, thereby possessing the best wear resistance.

3.4 Oxidation resistance

The XRD diffraction patterns of $(TiCrVAl)_{1-x}N_x$ coatings after 700 °C oxidation in air condition for 2 h are presented in Fig. 11 (a). After oxidation, the diffraction peaks corresponding to the high-entropy nitride FCC phase coexist with detectable oxide-related signals, indicating that the oxidation of the coating is activated at this temperature. To clearly resolve the multiple oxidation-related peaks in the low-angle region, the 20°-40° range in Fig. 11 (a) is magnified and displayed in Fig. 11 (b).

For the $(TiCrVAl)_{0.85}N_{0.15}$ and $(TiCrVAl)_{0.75}N_{0.25}$ coatings, the oxide peaks are identified as TiO_2 (ICCD PDF#21-1276) with peaks at 32° and 42.2° and $CrVO_4$ (ICCD PDF#38-1376) located at 22.3°, 25.1°, 28.3°, 30.5°, 37.4°, 41.7° and 42.6°, which are marked by red ellipses and blue circles, respectively. For the $(TiCrVAl)_{0.62}N_{0.38}$ coating, the oxidation products

shift to TiO_2, Cr_2O_3 (ICCD PDF#38-1479 appearing at 28.5° and 42.3°) and VO_2 (ICCD PDF#25-1003) that located at 30.6° and 42.3°. Moreover, a substantial decrease in the intensity of the oxide peaks is clearly observed. When the x is further increased to 0.43 and 0.46, in addition to the oxide phases of TiO_2, Cr_2O_3 and VO_2 that remain present, a new peak emerges at 22.2°. It corresponds to V_7O_{13} (ICCD PDF#18-1449) and its intensity increases noticeably. Typically, variations in the integrated intensity of oxide peaks reflect changes in the amount of volume oxidized, that is, a larger amount of volume oxidized corresponds to a stronger oxidation peak. Therefore, the evolution of oxide composition and peak intensity with increasing x value suggests that the oxidation resistance of the $(TiCrVAl)_{1-x}N_x$ coatings first improves and then deteriorates, reaching the strongest antioxidant capacity at x = 0.38.

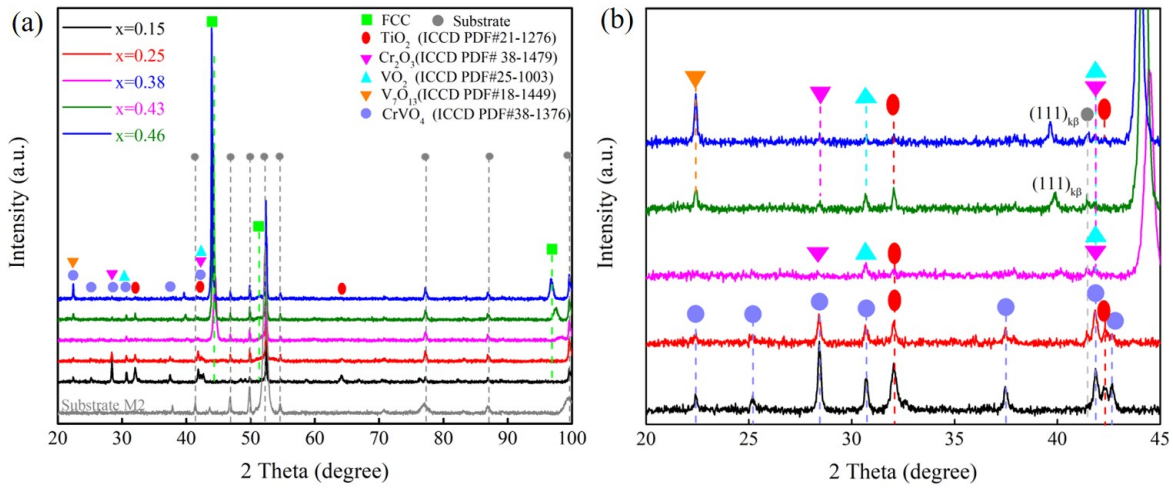

Figure 11. X-ray diffraction patterns of $(TiCrVAl)_{1-x}N_x$ coatings with x = 0.15-0.46 deposited on M2 substrates after 700 ˚C oxidation test in air conditions.

In addition to the emergence of oxide-related diffraction signals, it is also clearly observed that the underneath unoxidized FCC phase remains intact. Compared to the as-deposited coating, no detectable change is observed in the grain size of the FCC phase, indicating the excellent thermal stability of the $(TiCrVAl)_{1-x}N_x$ coating. This stability arises from the coupled effects of high-entropy effect and kinetic sluggish diffusion, which suppress grain growth and phase decomposition under high-temperature exposure [39][40]. In general, the in-situ microstructural evolution (i.e., grain coarsening) during oxidation induces in-situ changes in the effective diffusion coefficients of constituent elements and oxygen atoms, which in turn exerts complex and significant influences on the oxidation resistance of the coating [41][42]. However, for $(TiCrVAl)_{1-x}N_x$ coatings, their inherent thermal stability endows them with a stable structure, thereby eliminating the in-situ microstructural evolution during oxidation. Consequently, the dominant factor governing oxidation resistance of

$(TiCrVAl)_{1-x}N_x$ coating can be primarily attributed to the microstructure of the as-deposited coatings, which remains unchanged during oxidation.

Figure 12 presents the cross-sectional morphologies of the brittle-fractured $(TiCrVAl)_{1-x}N_x$ coatings in both the as-deposited and oxidized states. For the oxidized state of $(TiCrVAl)_{1-x}N_x$ coatings, the corresponding EDS elemental distribution maps covering Ti, Al, Cr, V, N, and O are provided in Fig. 13. In combination with XRD patterns, SEM morphologies and EDS element distributions, an overall trend can be discerned that the oxidation degree first decreases and then increases with x value. The thinnest oxide scale forms on the $(TiCrVAl)_{0.62}N_{0.38}$ coating, which corresponds to the optimal oxidation resistance. Besides, except for the fully oxidized $(TiCrVAl)_{0.85}N_{0.15}$ coating, the unoxidized portions of the remaining coatings retain their original as-deposited morphology, further demonstrating the thermal stability of the $(TiCrVAl)_{1-x}N_x$ coatings.

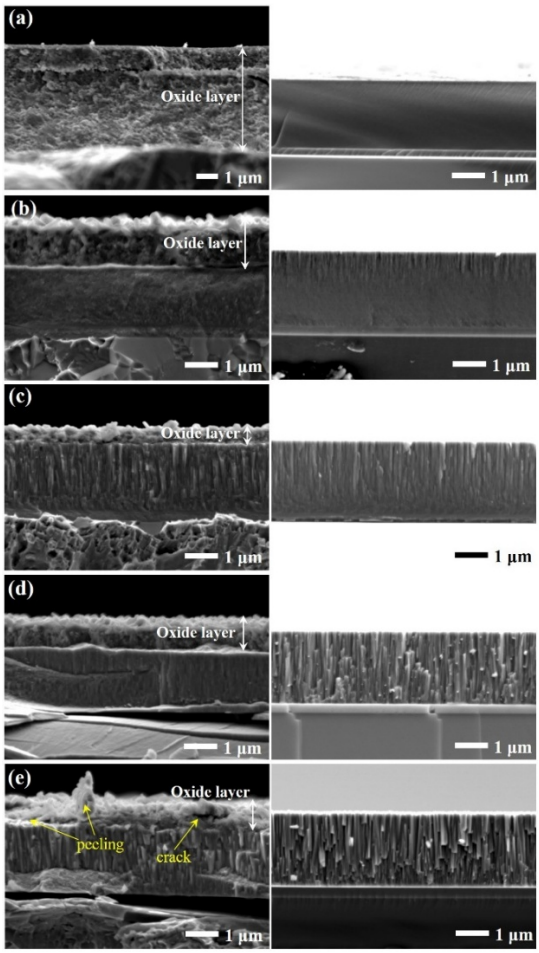

Figure 12. Cross-sectional SEM morphologes of $(TiCrVAl)_{1-x}N_x$ coatings with various x values deposited on M2 substrates after 2h oxidation, where the left column is the oxidized state and the right column is the deposited state: (a) x = 0.15, (b) x = 0.25, (c) x = 0.38, (d) x = 0.43 and (e) x = 0.46.

The oxide layers that form on the $(TiCrVAl)_{1-x}N_x$ coatings display distinctly different structural features, and the elemental species within these layers show nonuniform spatial distributions. When x = 0.15, the coating is completely oxidized after the oxidation test. It is likely associated with the higher free volume and more metal-enriched clusters within the coating, which provide fast diffusion pathways for the inward diffusion of oxygen, thereby leading to severe oxidation of the coating [43][44]. For $(TiCrVAl)_{0.75}N_{0.25}$ coating, the combination of SEM/EDS and XRD results indicates that the oxide layer exhibits a three-layer structure that consists of an outer TiO_2 layer, a discontinuous intermediate a-Al_2O_3 layer, and an inner $CrVO_4$ layer. This structure does not provide effective oxygen blocking and protective capability. Among them, the upper two layers are produced by the outward diffusion and subsequent oxidation of Ti and Al, confirmed by the Ti and Al element mappings in Fig. 13(b). The remaining oxide scale originates from the inward diffusion of oxygen and subsequent oxidation reactions with Cr and V. It is speculated that during the oxidation process, a-Al_2O_3 is formed first due to its strongest thermochemical oxygen affinity. However, as oxidation proceeds, a-Al_2O_3 layer is disrupted by the outward diffusion of Ti and the growth of TiO_2. Subsequently, a large amount of oxygen invades (sufficient oxygen partial pressure) and the $CrVO_4$ forms at the innermost layer. For the coatings with x = 0.15 and 0.25, it is confirmed that the types of oxidation products and corresponding oxidation reactions are identical. The difference lies in the fact that the intermediate oxides of the $(TiCrVAl)_{0.75}N_{0.25}$ coating persist for a longer duration and the overall oxide layer is thinner. The corresponding oxidation reactions can be described as follows.

$$4\,Al + 3\,O_2 \rightarrow 2\,Al_2O_3 \quad (1)$$

$$Ti + O_2 \rightarrow TiO_2 \quad (2)$$

$$4\,Cr + 3\,O_2 \rightarrow 2\,Cr_2O_3 \quad (3)$$

$$2\,V + O_2 \rightarrow 2\,VO \quad (4)$$

$$2\,V_2O_3 + O_2 \rightarrow 4\,VO_2 \quad (5)$$

$$Cr_2O_3 + 2\,VO_2 + \frac{1}{2}\,O_2 \rightarrow 2\,CrVO_4. \quad (6)$$

Among them, VO_2 and Cr_2O_3, represented by formulas (3)-(5), are transient phases and are not detected in XRD. Note that although the $(TiCrVAl)_{0.75}N_{0.25}$ coating is also amorphous, it displays significantly enhanced oxidation resistance compared to the $(TiCrVAl)_{0.85}N_{0.15}$ coating. It is well established that local coordination inhomogeneity and free volume in amorphous coatings constitute the diffusion channel for atom transport [45][46]. When the nitrogen content increases from 15 to 25 at.%, the stronger atomic-scale mismatch and the higher degree of lattice distortion lead to more inhomogeneous local coordination in the amorphous $(TiCrVAl)_{1-x}N_x$ coatings. This may reduce the local migration barrier of Al and promote its outward

diffusion, thereby facilitating the formation of a protective a-Al_2O_3 layer. Moreover, the higher nitrogen content reduces free volume and metal-rich clusters, helping to suppress the inward diffusion of oxygen. Additionally, high-nitrogen content coating is more prone to displacement oxidation (oxygen atoms replacing nitrogen atoms) [47], which has a higher activation energy, thus directly reducing the oxidation degree of the coating.

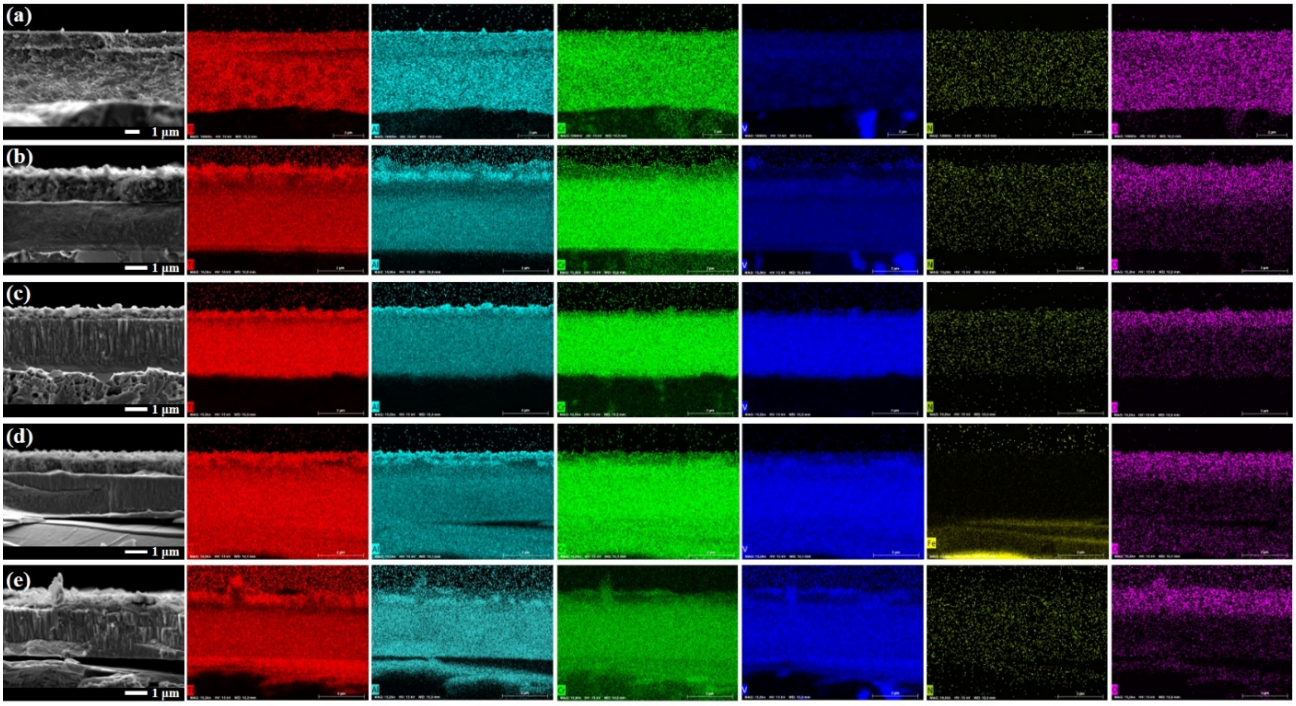

Figure 13. Cross-sectional SEM morphologies and corresponding elemental distribution maps of the $(TiCrVAl)_{1-x}N_x$ coatings deposited on M2 substrates after 2h oxidation test: (a) x = 0.15, (b) x = 0.25, (c) x = 0.38, (d) x = 0.43 and (e) x = 0.46.

When x increases to 0.38, the oxide layer on the coating surface becomes the thinnest, indicating the strongest oxidation resistance. Based on the phase constituents identified by XRD with the elemental distributions revealed by SEM/EDS, the oxide layer is inferred to possess a three-layer structure that consists of an outer continuous a-Al_2O_3 layer, a middle TiO_2 layer, and an inner V-rich oxides layer mixed with a small amount of Cr-oxides. The outermost single-phase continuous a-Al_2O_3 layer originates from the high chemical activity, rapid diffusion, and strong oxygen affinity of Al atoms. The TiO_2, VO_2, and small amounts of Cr_2O_3 formed sequentially in the middle and innermost parts are due to the chemical potential gradient driven by oxidation and the differences in the formation enthalpies of Ti, Cr, and V oxides, in which Ti oxides have the most negative formation enthalpy, followed by V oxides and subsequently Cr oxides. The relevant chemical reactions are shown in formulas (1)-(5). The dense and continuous a-Al_2O_3 layer provides excellent oxygen barrier properties, while other thermally grown oxides with crystalline structures offer relatively weak protection to the underlying coating. The formation of this protective oxide layer benefits from the nanocomposite structure of the $(TiCrVAl)_{0.62}N_{0.38}$ coating. In this

nanocomposite structure, the diffusion network consists of fine, discontinuous grain boundaries and phase boundaries. Therefore, the inward diffusion of environmental oxygen is hindered, resulting in a low oxygen partial pressure. The growth of Ti, Cr, and V oxides beneath the a-Al_2O_3 layer is thus insufficient to disrupt the continuity of the a-Al_2O_3 layer, thereby endowing the coating with excellent oxidation resistance.

When the nitrogen content further increases to x = 0.43 and 0.46, the oxide layer becomes thicker again, indicating a renewed deterioration in oxidation resistance. For the $(TiCrVAl)_{0.57}N_{0.43}$ coating, the oxide layer exhibits a two-layer structure that consists of an outer mixed TiO_2 and a-Al_2O_3 layer and an inner Cr-oxide and V-oxide layer, which are supplied by the outward diffusion of cations and the inward diffusion of oxygen, respectively. It is noted that the a-Al_2O_3 layer is non-uniform in thickness and intermixed with TiO_2, therefore resulting in insufficient protection. In the case of $(TiCrVAl)_{0.54}N_{0.46}$ coating, the oxide layer consists of an upper locally distributed Cr/V-oxide layer, a middle discontinuous layer comprising a-Al_2O_3 mixed with TiO_2, and a subsequent bottom layer of a-Al_2O_3 mixed with Cr/V-oxides. This structure provides even poorer oxygen-blocking protection. Furthermore, SEM reveals cracks and partial peeling of the oxide layer (yellow arrows in Fig. 12(e)), possibly caused by the mismatch of the thermal expansion coefficients between the complex, multi-layered oxide scale and the underlying coating. As x increases from 0.38 to 0.46, the $(TiCrVAl)_{1-x}N_x$ coating transitions to a fully crystallized structure, characterized by larger grain boundaries, coarser columnar crystals and more pronounced intercolumnar gaps. These characteristics facilitate the formation of penetrating diffusion pathways, increasing the diffusion path and diffusion rate of environmental oxygen into the interior, thereby leading to the degradation of oxidation resistance. For these two $(TiCrVAl)_{1-x}N_x$ coatings with x = 0.43 and 0.46, the oxidation products include Al_2O_3, TiO_2, Cr_2O_3, VO_2, and V_7O_{13}. Compared with the coating with x = 0.38, an additional chemical reaction occurs,

$$7\,VO_2 + \frac{1}{2}\,O_2 \rightarrow V_7O_{13}. \quad (7)$$

In summary, it can be concluded that for $(TiCrVAl)_{1-x}N_x$ coatings, the inherent nanocomposite structure that blocks oxygen diffusion, as well as the formation and maintenance of the single-phase, continuous a-Al_2O_3 layer, are the key determinants of oxidation resistance.

4. Conclusion

In the present work, high-entropy $(TiCrVAl)_{1-x}N_x$ coatings with controlled nitrogen contents (x = 0.15-0.46) were synthesized to elucidate the role of nitrogen-induced microstructure in controlling the mechanical, tribological, and oxidation properties of the coatings. With equiatomic metallic constituents, increasing nitrogen content drives a structural evolution from an amorphous state to a nanocomposite structure and ultimately to a fully crystallized structure. Concurrently, the

coating morphology transitions from a featureless state to columnar crystals with increasing coarseness. An intermediate nitrogen content of $x = 0.38$ ($(TiCrVAl)_{0.62}N_{0.38}$ coating) yields an optimized nanocomposite structure, leading to a favourable combination of high hardness, enhanced resistance to elastic and plastic deformation, and superior wear performance. Moreover, the strongest oxygen barrier performance was also achieved in the $(TiCrVAl)_{0.62}N_{0.38}$ coating, supported by the oxygen diffusion barrier provided by the nanocomposite structure and the formation and retention of the continuous single-phase a-Al_2O_3 layer. These results demonstrate that nitrogen content serves as a critical microstructural regulator in $(TiCrVAl)_{1-x}N_x$ coatings, enabling the simultaneous optimization of mechanical, tribological, and oxidation properties. Furthermore, it provides a design framework for next-generation protective coatings operating under harsh conditions.

Declaration of Competing Interest

The authors declare that they have no competing financial interests or personal relationships that could have appeared to influence the work reported in this paper.

Acknowledgments

The authors thank the National Natural Science Foundation of China [grant numbers 52401110], the National Natural Science Foundation of China [grant numbers 52302047], and the project ZR2024MF053 supported by Shandong Provincial Natural Science Foundation for their financial support of this study.

References

[1] M.L. Grilli, D. Valerini, A.E. Slobozeanu, B.O. Postolnyi, S. Balos, A. Rizzo, R.R. Piticescu, Critical raw materials saving by protective coatings under extreme conditions: A review of last trends in alloys and coatings for aerospace engine applications, Materials 14 (7) (2021) 1656. https://doi.org/10.3390/ma14071656

[2] B. Zhao, Y. Wang, J. Peng, X. Wang, W. Ding, X. Lei, R. Das, Overcoming challenges: advancements in cutting techniques for high strength-toughness alloys in aero-engines, Int. J. Extreme Manuf. 6 (6) (2024) 062012. https://doi.org/10.1088/2631-7990/ad8117

[3] H. Wang, Z. Chen, J. Huang, L. Quan, B. Zhao, Development of high-speed on-off valves and their applications, Chin. J. Mech. Eng. 35 (1) (2022) 67. https://doi.org/10.1186/s10033-022-00720-5

[4] O. Bazaluk, A. Velychkovych, L. Ropyak, M. Pashechko, T. Pryhorovska, V. Lozynskyi, Influence of heavy weight drill pipe material and drill bit manufacturing errors on stress state of steel blades, Energies 14 (14) (2021) 4198. https://doi.org/10.3390/en14144198

[5] H. Cao, H. Li, F. Liu, W. Luo, F. Qi, N. Zhao, B. Liao, Microstructure, mechanical and tribological properties of multilayer TiAl/TiAlN coatings on Al alloys by FCVA technology, Ceram. Int. 48 (4) (2022) 5476–5487. https://doi.org/10.1016/j.ceramint.2021.11.092

[6] L. Chavee, E. Serag, M. da Silva Pires, S. Lucas, E. Haye, A mechanistic approach of oxidation resistance, structural and mechanical behaviour of TiAlN coatings, Appl. Surf. Sci. 586 (2022) 152851. https://doi.org/10.1016/j.apsusc.2022.152851

[7] H. Guo, Q.D. Sun, M. Zhou, Y. Yu, Q. Wang, X.L. Wang, Erosion behavior of CrN, CrAlN and CrAlN/CrN multilayer coatings deposited on Ti6Al4V, Surf. Coat. Technol. 437 (2022) 128284. https://doi.org/10.1016/j.surfcoat.2022.128284

[8] V. Novikov, N. Stepanov, S. Zherebtsov, G. Salishchev, Structure and properties of high-entropy nitride coatings, Metals 12 (5) (2022) 847. https://doi.org/10.3390/met12050847

[9] H.D. Zhang, J.W. Du, Y.X. Xu, S.Q. Wang, L. Chen, Structure and thermomechanical properties of superlattice-stabilized TiNbTaZrSiAlN high-entropy coating, J. Alloys Compd. 994 (2024) 174736. https://doi.org/10.1016/j.jallcom.2024.174736

[10] H. Luo, M.A.P. Yazdi, S.C. Chen, H. Sun, F. Gao, O. Heintz, Structure, mechanical and tribological properties, and oxidation resistance of TaC/aC:H films deposited by high power impulse magnetron sputtering, Ceram. Int. 46 (16) (2020) 24986-25000. https://doi.org/10.1016/j.ceramint.2020.04.047

[11] D.C. Tsai, Z.C. Chang, B.H. Kuo, M.H. Shiao, S.Y. Chang, F.S. Shieu, Structural morphology and characterization of (AlCrMoTaTi)N coating deposited via magnetron sputtering, Appl. Surf. Sci. 282 (2013) 789-797. https://doi.org/10.1016/j.apsusc.2013.06.153

[12] D.C. Tsai, M.J. Deng, Z.C. Chang, B.H. Kuo, E.C. Chen, S.Y. Chang, et al., Oxidation resistance and characterization of (AlCrMoTaTi)-Six-N coating deposited via magnetron sputtering, J. Alloys Compd. 647 (2015) 179-188. https://doi.org/10.1016/j.jallcom.2015.05.222

[13] V. Braic, A. Vladescu, M. Balaceanu, C.R. Luculescu, M. Braic, Nanostructured multi-element (TiZrNbHfTa)N and (TiZrNbHfTa)C hard coatings, Surf. Coat. Technol. 211 (2012) 117-121. https://doi.org/10.1016/j.surfcoat.2012.09.024

[14] D. Xu, J. Xu, Q. Zhou, Y. Zhao, Q. Wang, J. Wu, et al., Role of microstructure, mechanical performance, and adhesion

on cavitation erosion resistance of a nanocrystalline (TiZrNbTaMo)N refractory high-entropy nitride coating on TC4 alloy, Mater. Today Commun. (2025) 114025. https://doi.org/10.1016/j.mtcomm.2025.114025

[15] R. Chen, Z. Cai, J. Pu, Z. Lu, S. Chen, S. Zheng, et al., Effects of nitriding on the microstructure and properties of VAlTiCrMo high-entropy alloy coatings by sputtering technique, J. Alloys Compd. 827 (2020) 153836. https://doi.org/10.1016/j.jallcom.2020.153836

[16] Y. Si, G. Wang, M. Wen, Y. Tong, W. Wang, Y. Li, et al., Corrosion and friction resistance of TiVCrZrWN_x high-entropy ceramics coatings prepared by magnetron sputtering, Ceram. Int. 48 (7) (2022) 9342-9352. https://doi.org/10.1016/j.ceramint.2021.12.258

[17] C.Y. Lai, Y.I. Chen, Structural, mechanical, and anticorrosive properties of (TiZrNbTa)N_x films, J. Mater. Res. Technol. 26 (2023) 8327-8336. https://doi.org/10.1016/j.jmrt.2023.08.084

[18] H. Luo, H. Sun, L. Yuan, P. Wang, X. Zhao, P. Briois, et al., Tailoring the microstructure, mechanical and tribological properties and oxidation resistance of (AlTiCrVTa)N_x coatings by controlling nitrogen content, Ceram. Int. 50 (9) (2024) 16027-16037. https://doi.org/10.1016/j.ceramint.2024.02.207

[19] J.T. Gudmundsson, Physics and technology of magnetron sputtering discharges, Plasma Sources Sci. Technol. 29 (11) (2020) 113001. https://doi.org/10.1088/1361-6595/abb8a3

[20] J.T. Gudmundsson, A. Anders, A. von Keudell, Foundations of physical vapor deposition with plasma assistance, Plasma Sources Sci. Technol. 31 (8) (2022) 083001. https://doi.org/10.1088/1361-6595/ac7c88

[21] Y. Xu, G. Li, Y. Xia, Synthesis and characterization of super-hard AlCrTiVZr high-entropy alloy nitride films deposited by HiPIMS, Appl. Surf. Sci. 523 (2020) 146529. https://doi.org/10.1016/j.apsusc.2020.146529

[22] W.L. Hsu, C.W. Tsai, A.C. Yeh, J.W. Yeh, Clarifying the four core effects of high-entropy materials, Nat. Rev. Chem. 8 (6) (2024) 471-485. https://doi.org/10.1038/s41570-024-00619-6

[23] X.H. Yan, J.S. Li, W.R. Zhang, Y. Zhang, A brief review of high-entropy films, Mater. Chem. Phys. 210 (2018) 12-19. https://doi.org/10.1016/j.matchemphys.2018.02.029

[24] C. Zhang, X. Lu, H. Zhou, Y. Wang, X. Sui, Z. Shi, et al., Construction of a compact nanocrystal structure for (CrNbTiAlV)N_x high-entropy nitride films to improve the tribo-corrosion performance, Surf. Coat. Technol. 429 (2022) 127921. https://doi.org/10.1016/j.surfcoat.2021.127921

[25] D.C. Tsai, Y.L. Huang, S.R. Lin, S.C. Liang, F.S. Shieu, Effect of nitrogen flow ratios on the structure and mechanical properties of (TiVCrZrY)N coatings prepared by reactive magnetron sputtering, Appl. Surf. Sci. 257 (4) (2010)

1361-1367. https://doi.org/10.1016/j.apsusc.2010.08.088

[26] S. Mustapha, M.M. Ndamitso, A.S. Abdulkareem, J.O. Tijani, D.T. Shuaib, et al., Comparative study of crystallite size using Williamson-Hall and Debye-Scherrer plots for ZnO nanoparticles, Adv. Nat. Sci.: Nanosci. Nanotechnol. 10 (4) (2019) 045013. https://doi.org/10.1088/2043-6254/10/4/045013

[27] R. Sharma, D.P. Bisen, U. Shukla, B.G. Sharma, X-ray diffraction: a powerful method of characterizing nanomaterials, Recent Res. Sci. Technol. 4 (8) (2012).

[28] H. Li, N. Jiang, J. Li, J. Huang, J. Kong, D. Xiong, Hard and tough (NbTaMoW)Nx high-entropy nitride films with sub-stoichiometric nitrogen, J. Alloys Compd. 889 (2021) 161713. https://doi.org/10.1016/j.jallcom.2021.161713

[29] X. Lu, C. Zhang, X. Zhang, X. Cao, J. Kang, X. Sui, et al., Dependence of mechanical and tribological performance on the microstructure of (CrAlTiNbV)Nx high-entropy nitride coatings in aviation lubricant, Ceram. Int. 47 (19) (2021) 27342-27350. https://doi.org/10.1016/j.ceramint.2021.06.239

[30] A. Anders, Discharge physics of high power impulse magnetron sputtering, Surf. Coat. Technol. 205 (2011) S1-S9. https://doi.org/10.1016/j.surfcoat.2010.11.067

[31] D. Depla, S. Mahieu, R. De Gryse, Magnetron sputter deposition: Linking discharge voltage with target properties, Thin Solid Films 517 (9) (2009) 2825-2839. https://doi.org/10.1016/j.tsf.2009.01.154

[32] C. Zhang, X. Lu, C. Wang, X. Sui, Y. Wang, H. Zhou, et al., Tailoring the microstructure, mechanical and tribocorrosion performance of (CrNbTiAlV)N_x high-entropy nitride films by controlling nitrogen flow, J. Mater. Sci. Technol. 107 (2022) 172-182. https://doi.org/10.1016/j.jmst.2021.10.036

[33] J. Li, Y. Chen, Y. Zhao, X. Shi, S. Zhang, Super-hard (MoSiTiVZr)N_x high-entropy nitride coatings, J. Alloys Compd. 926 (2022) 166807. https://doi.org/10.1016/j.jallcom.2022.166807

[34] K. Xiong, L. Yang, F. Wang, S. Zhang, L. You, H. Wu, et al., A first-principles study of the effects of nitrogen on lattice distortion, mechanical and electronic properties of (ZrHfNbTa)$C_{1-x}N_x$ high-entropy carbonitrides, J. Alloys Compd. 930 (2023) 167378. https://doi.org/10.1016/j.jallcom.2022.167378

[35] M.H. Hsieh, M.H. Tsai, W.J. Shen, J.W. Yeh, Structure and properties of two Al-Cr-Nb-Si-Ti high-entropy nitride coatings, Surf. Coat. Technol. 221 (2013) 118-123. https://doi.org/10.1016/j.surfcoat.2013.01.028

[36] M. Khadem, O.V. Penkov, H.K. Yang, D.E. Kim, Tribology of multilayer coatings for wear reduction: A review, Friction 5 (3) (2017) 248-262. https://doi.org/10.1016/j.friction.2017.06.001

[37] A. Leyland, A. Matthews, On the significance of the H/E ratio in wear control: a nanocomposite coating approach to

optimised tribological behaviour, Wear 246 (1-2) (2000) 1-11. https://doi.org/10.1016/S0043-1648(00)00488-9

[38] D. Luo, Q. Zhou, Z. Huang, Y. Li, Y. Liu, Q. Li, et al., Tribological behavior of high-entropy alloy coatings: a review, Coatings 12 (10) (2022) 1428. https://doi.org/10.3390/coatings12101428

[39] P. H. Mayrhofer, A. Kirnbauer, P. Ertelthaler, C. M. Koller, High-entropy ceramic thin films; A case study on transition metal diborides, Scripta Materialia 149 (2018) 93-97. https://doi.org/10.1016/j.scriptamat.2018.02.008

[40] R. Li, M. Li, C. Jiang, B. Qiao, W. Zhang, J. Xu, Thermal stability of AlCrTaTiZrMo-nitride high-entropy film as a diffusion barrier for Cu metallization, J. Alloys Compd. 773 (2019) 482-489. https://doi.org/10.1016/j.jallcom.2018.10.073

[41] J. Wang, M. Chen, L. Yang, W. Sun, S. Zhu, F. Wang, Nanocrystalline coatings on superalloys against high temperature oxidation: A review, Corros. Commun. 1 (2021) 58-69. https://doi.org/10.1016/j.corcom.2021.01.006

[42] Y. Karanth, S. Sharma, K. Darling, H. El Kadiri, K. Solanki, Oxidation behavior of nanocrystalline alloys, Materials 17 (23) (2024) 5842. https://doi.org/10.3390/ma17235842

[43] F.G. Shi, T.G. Nieh, Y.T. Chou, A free volume approach for self-diffusion in metals, Scripta Mater. 43 (3) (2000) 265-267. https://doi.org/10.1016/S1359-6462(00)00420-6

[44] H. Schmidt, M. Gupta, M. Bruns, Nitrogen diffusion in amorphous silicon nitride isotope multilayers probed by neutron reflectometry, Phys. Rev. Lett. 96 (5) (2006) 055901. https://doi.org/10.1103/PhysRevLett.96.055901

[45] F. Müller-Plathe, Diffusion of penetrants in amorphous polymers: A molecular dynamics study, J. Chem. Phys. 94 (4) (1991) 3192-3199. https://doi.org/10.1063/1.459792

[46] S. Flege, U. Fecher, H. Hahn, Diffusion in amorphous NiZrAl alloys, J. Non-Cryst. Solids 270 (1-3) (2000) 123-128. https://doi.org/10.1016/S0022-3093(00)00023-4

[47] D.H. Ma, H.J. Wang, M. Niu, J.B. Wen, H. Wei, J. Zhou, D.H. Zhang, Oxidation behavior of amorphous silicon nitride nanoparticles, Ceram. Int. 44 (2) (2018) 1443-1447. https://doi.org/10.1016/j.ceramint.2017.09.206